RSC Advances

PAPER

View Article Online
View Journal | View Issue

Cite this: *RSC Adv.*, 2022, **12**, 31535

Simple fluorescence chemosensor for the detection of calcium ions in water samples and its application in bio-imaging of cancer cells†

Maral Salek-Maghsoodi,[a] Zahra Golsanamlu,[a] Sanam Sadeghi-Mohammadi,[b] Masoud Gazizadeh,[c] Jafar Soleymani *[a] and Reza Safaralizadeh[d]

Received 2nd August 2022
Accepted 29th October 2022

DOI: 10.1039/d2ra04815a

rsc.li/rsc-advances

This article describes the design, synthesis and characterization of a sensor suitable for practical measurement of ionized calcium in water samples and cancer cells. Calcium is an important ion in living organs and works as a messenger in several cellular functions. A lack of Ca ions interrupts the immune system and can lead to several diseases. A novel magnetic-polydopamine nanoparticle (PDNP)/rhodamine B (RhB)/folic acid (FA) nanoparticle was developed for the determination of calcium ions in MCF 7 cell lysates and water samples. Furthermore, the produced nanoparticle was employed for bioimaging of folate receptor (FR)-overexpressed cancer cells. This nanoprobe displayed a bright photoluminescence emission at 576 nm under an excitation wavelength of 420 nm. In the presence of calcium ions, the fluorescence emission of the MNPs-PDNPs/RhB/FA probe was proportionally decreased from 20 ng mL^{-1} to 100 ng mL^{-1} and 0.5 μg mL^{-1} to 20 μg mL^{-1} with a lower limit of quantification (LLOQ) of about 20 ng mL^{-1}. The developed sensor showed a low-interference manner in the presence of possible coexistence interfering ions. In addition, this nanomaterial showed excellent biocompatibility with favorable differentiation ability to attach to the FR-positive cancer cells. The MNPs-PDNPs/RhB/FA nanoparticle has been utilized for bioimaging of the MCF 7 cell with favorable differentiation ability.

1. Introduction

Calcium ions (Ca^{2+}) are the most ubiquitous signaling molecules in living organisms, regulating numerous biological functions. Calcium is a vital ion in living organs and elaborates as an extracellular messenger in several cellular functions. Lack of Ca^{2+} interrupts the immune system and leads to several diseases.[1] The dysregulation of calcium concentration in cells is related to some neurodegenerative disorders of Alzheimer's disease (AD), Parkinson's disease (PD), and Huntington's disease (HD).[2–4] Furthermore, some evidence proposes that an abnormal level of calcium is associated with the progress of cancer. Also, the concentration of Ca^{2+} in environmental sources must be controlled to regulate its concentrations in water and soil.[5]

Recently, monitoring of intracellular concentrations of cationic and anionic ions has received great attention to be employed as an indicator for early-stage detection of the corresponded disorders.[6,7] Hence, the design of a calcium sensing platform is extremely needed for its reliable detection in various biological and environmental samples. To date, there have been reported several analytical techniques for measuring and detection of Ca^{2+} including electrochemical method, NMR analysis, electrochemical, atomic spectroscopy, colorimetric (UV), and photoluminescence methods in diverse samples which offer specific, sensitive, and reliable detection.[7–10] However, some disadvantages have been found for these techniques such as laborious detection approaches, high-cost instrumentation, and nonsufficient sensitivity and selectivity associated with atomic spectroscopy-based methods, fragile instrumentation and time consuming manipulations associated with electrochemical methods, the high detection limit with colorimetric techniques, and *etc.* These restrictions limit their uses for the fast detection of calcium ions. In recent years, fluorescence and electrochemical-based sensor systems for Ca^{2+} detection have attracted great attentions owing to their operational simplicity and real-time detection, *etc.*, that have been widely utilized for the detection of various analytes due to their favorable analytical performance of high sensitivity, fast analysis time, and non-destructive detection approaches.[8–15]

[a]*Pharmaceutical Analysis Research Center, Tabriz University of Medical Sciences, Tabriz, Iran. E-mail: jsoleymanii@gmail.com; soleymanij@tbzmed.ac.ir; Tel: +98 41 3337 5365*

[b]*Tuberculosis and Lung Diseases Research Center, Tabriz University of Medical Sciences, Tabriz, Iran*

[c]*Liver and Gastrointestinal Research Center, Tabriz University of Medical Sciences, Tabriz, Iran*

[d]*Department of Biology, Faculty of Natural Sciences, Tabriz University, Tabriz, Iran*

† Electronic supplementary information (ESI) available. See DOI: https://doi.org/10.1039/d2ra04815a

Fluorescent materials not only showed potential fluorescent probes for the determination of ions in live cells and they also could be applied for the cancer cells bioimaging. There has been a growing request to use these materials in bioimaging applications alongside previously used techniques such as computed tomography (CT), single-photon emission computed tomography (SPECT), magnetic resonance imaging (MRI), *etc.* for *in vivo* bioimaging. The fluorescence-based bioimaging exhibited several beneficial features of high safety, simplicity, sensitivity, and biocompatibility nature toward living cells.[16,17] The detection of biomolecular cellular functions using fluorescent materials is becoming much easier owing to their intensive development for biosensing and medical applications. Because, several human diseases, including various cardiomyopathies, neurodegenerative diseases, and cancer are known to be associated with altered Ca^{2+} concentration. There is a strong need to develop Ca^{2+} sensors capable of real-time quantitative Ca^{2+} concentration measurements in specific subcellular environments. Current estimates of Ca^{2+} have been derived using major types of Ca^{2+} indicators and sensors like (1) synthetic small molecule fluorescent indicators, (2) specifically modified derivatives of the chemiluminescent protein, (3) fluorescent indicators based on green fluorescence protein, and (4) some small molecule dyes accumulate in certain cellular compartments of cells.

Bioimaging of cancer cells is implemented by different approaches that the targeted imaging is the best one to differentiate cancer cells from normal cells. However, targeted bioimaging could be done by biological agents like antibody–antigen, aptamers, *etc.*, or by chemical moieties like folic acid (FA), hyaluronic acid, *etc.* functionalized agents. Despite the high specificity of the biological agents for bioimaging, these substances are high-cost, low stable, and usually, severe conditions are needed to be applied for the storing of them. Employing simple techniques like fluorescence and electrochemical methods provide more versatile and facile approaches for bioimaging aims.[18,19]

FA molecules have been utilized as labeling molecules for the modification of various molecules and nanoparticles for different medical aims.[20,21] FA-functionalized materials are very selective toward folate receptor (FR) of the surface membrane of some of the FRs-overexpressed cancer cells.[22] To date, diverse new materials including metallic (gold, silver, *etc.*)-based, carbon-based, silica-based nanoparticles, *etc.* have been modified with FA molecules.[23–26]

Herein, the use of the magnetic-poly dopamine nanoparticles (PDNPs)/rhodamine B (RhB)/FA was presented for the facile determination of calcium ions in water samples, and cell lysates. Furthermore, the MNPs-PDNPs/RhB/FA nanoparticles were also employed for the bioimaging and measuring of intracellular calcium ions at trace levels. The MNPs-PDNPs/RhB/FA-based probe showed high selectivity towards calcium ions in the presence of metal ions. The developed fluorescent calcium sensor displayed good water dispersity and biocompatibility. Additionally, this novel nanoprobe has been utilized for the determination of calcium ions in MCF 7 cell lysates as well as the detection of calcium ions in water samples from different sources.

2. Experimental section

2.1. Materials

FA was obtained from Mehr Darou pharmaceutical company (Iran). 3-(4,5-Dimethylthiazol-2-yl)-2,5-diphenyltetrazolium bromide (MTT), 1-ethyl-3-(3-dimethylaminopropyl)carbodiimide (EDC, 98.0%), rhodamine B (RhB, 98.0%), and *N*-hydroxysuccinimide (NHS, 98.0%) were purchased from Sigma-Aldrich (USA). Dimethylsulfoxide (DMSO, 98.3%), ammonia solution (15%), sodium hydroxide (NaOH, 98.0%), and hydrochloric acid (HCl, 35.5%) were provided from Merck company (Germany). Also, sodium acetate, sodium dihydrogen phosphate, disodium hydrogen phosphate, acetic acid, and trisaminomethane hydrochloride (Tris-HCl) were purchased from Merck (Germany). Cell culture materials *i.e.* Roswell Park Memorial Institute (RPMI) 1640, trypsin–EDTA (25%), fetal bovine serum (FBS), and penicillin/streptomycin were obtained from Gibco Co. (UK). MCF 7 and HEK 293 cell lines were obtained from National Cell Bank of Iran (NCBI) (Iran).

2.2. Apparatus

Fourier transform infrared (FTIR) spectra were recorded using Bruker model instrument (Billerica, Massachusetts, US). A JASCO FP 750 spectrofluorometer (Tokyo, Japan) was employed to record fluorescence emission spectra. The size and surface charge of the MNPs-PDNPs/RhB/FA nanoparticles were characterized by Malvern particle size analyzer (Malvern, UK). Field emission scanning electron microscopy (FE-SEM, FEG-SEM MIRA3 TESCAN, Brno, Czech Republic) was used to show the morphology and analyze the energy dispersive X-ray (EDX) spectrum of the MNPs-PDNPs/RhB/FA nanoparticles. Atomic force microscopy (AFM) was employed to study surface topography of the MNPs-PDNPs/RhB/FA through a Digital Instruments nanosurf mobile S (Grammetstrasse, Switzerland). Crystallographic structure of the MNPs-PDNPs/RhB/FA was verified using X-ray diffraction (XRD) technique using Siemens D 5000 X-ray diffractometer (Texas, USA) with a CuKα anode ($\lambda = 1.54$ Å, 40 kV, 30 mA). The magnetic property was determined by MDKB (Kashan, Iran). The cellular internalization of the MNPs-PDNPs/RhB/FA nanoparticles was recorded by fluorescent microscopy (Olympus BX64, Olympus, Japan) with U-MWU2 fluorescence filter (excitation filter BP 330e385, dichromatic mirror DM 400, emission filter LP 420). A microplate reader (Awareness Technology, Florida, USA) was utilized to measure absorbance of MTT assay.

2.3. Synthesis

2.3.1. Synthesis of magnetic particles (MNPs). Briefly, 3.24 g of $FeCl_3$ and 2.76 g of $FeSO_4$ were dissolved in 20 mL of water. Then, 1.5 mL of HCl was added and stirred (6000 rpm) to complete the dissolving process. Next, 100 mL of NaOH (1.25 M) were added dropwise under stirring conditions for 30 min. Final back color magnetic materials are collected by centrifuging, and

several times were washed with pure water to remove to reach pH = 7.

2.3.2. Preparation of PDNPs. 500 mg of as-prepared magnetic particles were dispersed in 25 mL of PBS buffers at pH = 8.5 and sonicated for at least 30 min to obtain a homogenized dispersion. At the end of the dispersion period, the pH of the solution was controlled and adjusted to pH 8.5. Then, an appropriate amount of dopamine (DA) (47.5 mg) was added to reach the concentration of 10 mM. The mixture is mechanically agitated for 3 h to complete the polymerization of DA on the surface of magnetic nanoparticles. After then, 200 μL of ethylenediamine was added to the mixture to change the magnetic microparticles of DA to the MNPs-PDNPs. The EDA molecules induce the degradation of PDA non-fluorescent particles to the highly florescent PDNPs. These molecules showed reductive properties which made high yields PDNPs. Degradation of PDA particles not only decreases their final sizes but can enhance the water solubility and dispersibility of particles. It is proposed that degradation of the aggregated PDA particles causes to a reduction the π–π interactions between PDA particles.[27,28] Finally, as-prepared MNPs-PDNPs were washed several times with water and stored in a refrigerator for further use.

2.3.3. Synthesis RhB-NHS and FA-NHS. The carboxylic groups of the RhB molecules are activated by EDC/NHS-coupling method. Briefly, 3 mg of RhB, 5 mg of NHS, and 4 mg of EDC were dissolved in 10 mL of PBS buffer solution with a pH of 7.0 and stirred (600 rpm) for 12 h at room temperature. Finally, the RhB-NHS molecules were used to attach to the amine groups of the PDNPs. The same approach was applied to the activation of FA molecules.

2.3.4. Synthesis of MNPs-PDNPs/RhB/FA. 5 mg of MNPs-PDNPs was added to 5 mL of RhB-NHS and then another 5 mL of FA-NHS was supplemented and stirred (600 rpm) at room temperature for 6 h. A competition was initiated between RhB-NHS and FA-NHS molecules to attach to the amine groups of PDNPs. The as-produced MNPs-PDNPs/RhB/FA nanoparticles were purified using a dialysis bag (molecular weight cutoff 3 kDa) against distilled water to remove the unreacted reagents. The as-prepared MNPs-PDNPs/RhB/FA nanoparticles are stored in a refrigerator for the next uses. All synthesis approaches are demonstrated in Scheme 1.

2.4. Biological section

2.4.1. Cell culture. The cell lines were cultured in the RPMI 1640 medium (10% of FBS and 1% penicillin/streptomycin) at the 25 mL flasks and then incubated for days to grow. Upon reaching the cell population of 80%, the RPMI media was discarded and washed with phosphate buffer solution (PBS, pH 7.4). Next, EDTA–trypsin solution was poured into the flask to detach the cells from the bottom of the flasks. Then, the cell suspension was transported to a tube and centrifuged to separate the cells. Finally, fresh FBS-supplemented RPMI was added to the cells.

2.4.2. Cell viability. The cell viability of MNPs-PDNPs/RhB/FA nanoparticles towards the cell lines was measured by MTT assay. 10^4 of MCF 7 cancer cells were added into the wells of a 96-well plate and then incubated for 24 h. Next, different concentrations of the MNPs-PDNPs/RhB/FA nanoparticles (5–500 μg mL^{-1}) were added to the wells and incubated for 6, 24, and 48 h. Then, the MTT reagent (20 μL of 3 mg mL^{-1}) was added to the wells and incubated for 4 h. Next, the wells media were poured out and 200 μL of absolute DMSO were added and incubated for 30 min. Finally, the absorbances of the wells were recorded at 570 nm and the relative cell viabilities were calculated against the control groups.

2.4.3. Cell uptake. The cell internalization of the MNPs-PDNPs/RhB/FA nanoparticles to the FR-positive (MCF 7) and negative (HEK-293) cell lines was investigated with various concentrations of nanoparticles. 5×10^5 of the cells were added to a 6-wells plate. After 24 h, the MNPs-PDNPs/RhB/FA nanoparticles were added to the wells. Next, the internalization value was evaluated by fluorescence microscopy.

2.4.4. Bioimaging of calcium ions in live cells. Fluorescence bioimages of the MNPs-PDNPs/RhB/FA nanoparticles treated MCF 7 cells that incubated with different concentrations of Ca ions were recorded. 5×10^5 of MCF 7 cells were added into the wells of a 6-well plate and subsequently incubated for 24 h. Next, the cells were incubated with various concentration of calcium ions (5, 20, and 50 μg mL^{-1}) for 6 h. Next, MNPs-PDNPs/RhB/FA nanoparticles were added to the wells and incubated for 4 h. Then, fluorescence images were captured in the absence and presence of calcium ions.

2.4.5. Detection of Ca ions in cell lysates. Different amounts of calcium ions were added to the MCF 7 cells and incubated for 24 h to sufficient uptake to the cells. Then supernatant RPMI was poured out and the cells were placed in a centrifuge tube to lysate the cancer cells at the high centrifuging speed (10 000 rpm). Then, the solution was treated with HCl (1 M). Finally, the supernatant was separated by a centrifuge and the amount of calcium was determined with the designed probe.

2.5. Pretreatment of water samples

Tap water, commercial mineral, and Aras river water samples were collected from the local sources and then filtrated to delete possible particles. Then, suitable volumes were added to the probe *i.e.* the MNPs-PDNPs/RhB/FA nanoparticles at the optimized condition and fluorescence emissions were recorded by a fluorescence technique. The final concentrations of calcium ions were determined using a previously plotted calibration curve which was already provided in water media.

3. Results and discussion

3.1. Characterization of MNPs-PDNPs/RhB/FA nanomaterials

Fig. 1 displays the TEM and FE-SEM images of MNPs-PDNPs/RhB/FA nanoparticles. It is clear that the general shape of the MNPs-PDNPs/RhB/FA nanoparticles is spherical. The MNPs-PDNPs/RhB/FA nanoparticles size were computed from TEM and FE-SEM images using ImageJ 21.1 ± 6.3. Also, AFM analysis confirmed the topography of the nanoparticles as determined

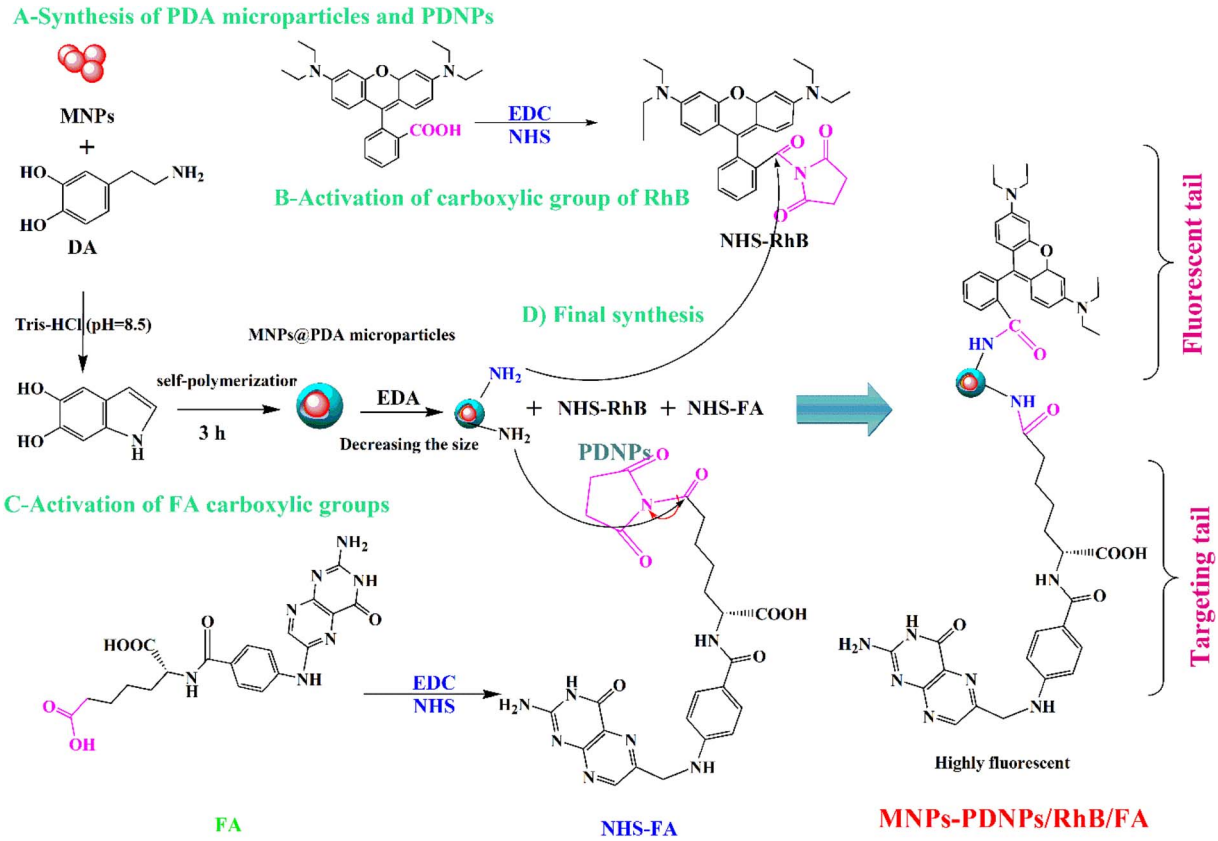

Scheme 1 Synthesis approach of the MNPs-PDNPs/RhB/FA nanoparticles.

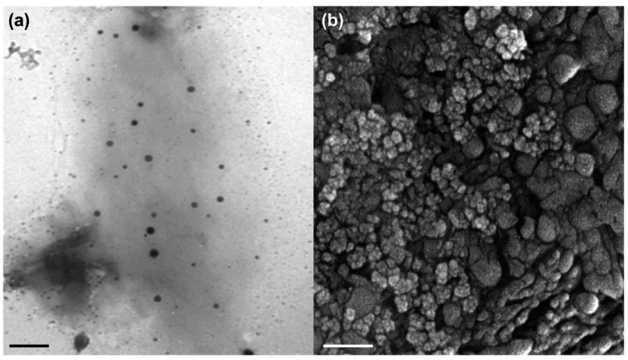

Fig. 1 (a) TEM, and (b) FE-SEM images of the MNPs-PDNPs/RhB/FA nanoparticles (scale bar = 50 nm).

by FE-SEM and TEM techniques (Fig. S1†). The size of MNPs-PDNPs/RhB/FA nanoparticles is inconsistent with the hydrated diameter obtained by dynamic light scattering (DLS) techniques (Fig. S2a†). To observe the surface charge, the MNPs-PDNPs/RhB/FA zeta potential was determined as +17.9 mV (Fig. S2b†) which is largely affected by PDNPs with a zeta potential of +102.0 mV.[29] Generally, amine groups turned to their cationic forms at low and neutral pHs. Also, the addition of FA molecules with negative zeta potential, influenced the final zeta potential to the negative values. The +17.9 mV zeta potential shows how stable during the colloidal phase. Stable colloidal dispersions are obtained at relatively high zeta. In other words, if the particles in any suspension possess large zeta potential values (negative or positive) then they tend to repulse each other with no desire to produce coagulation.

The elemental composition analysis of the MNPs-PDNPs/RhB/FA nanoparticles was carried out using energy dispersive X-ray (EDX) analysis equipped with FE-SEM, and showed that the percentages of carbon, nitrogen, oxygen, and ferric/ferrous ions of 20.21%, 25.19%, 31.75%, and 22.85%, respectively (Fig. S3 and Table S1†). The obtained results confirm the presence of the elements which must be available on the final structure of the MNPs-PDNPs/RhB/FA nanoparticles.

The surface functional groups of the MNPs-PDNPs/RhB/FA nanoparticles and FA molecules were detected by FTIR (Fig. S4†). An absorption peak at around 550 cm^{-1} confirms the presence of the Fe–O bonds.[30] The attachment of FA and RhB molecules to the surface of PDNPs could be observed between 1200–1800 cm^{-1} and 100–500 cm^{-1}, respectively. The presence of amide groups is confirmed by the 3350 and 1651 cm^{-1} spectra which confirms the attachment of RhB and FA molecules to the amine-functionalized PDNPs.[31,32] It is noteworthy that the formation of amide bonds is one of the main confirmations in the EDC/NHS coupling reactions.[33]

Magnetic property of the MNPs-PDNPs/RhB/FA was measured and shown in Fig. S5.† The saturation magnetization of the nanocomposite was found equal to 3.0 emu g^{-1}, showing favorable magnetic property of the MNPs-PDNPs/RhB/FA. In

Fig. S5,† it clear that by increasing the magnetic field −10 to +10 T, the magnetization enhanced severely with forming an S-like curve. Usually, materials with large magnetic properties showed higher magnetization value, however, the magnetic properties of the MNPs-PDNPs/RhB/FA is logically limited as compared with bare MNPs with magnetization value of around 39.5 emu g^{-1}.[34] The crystallographic structure of the MNPs-PDNPs/RhB/FA was also checked by the XRD technique at the 2θ range from 4–80° Fig. S6.† It is evidently observed that the MNPs-PDNPs/RhB/FA do not have sharp diffraction peaks which is a typical spectrum for amorphous or ultrafine crystalline materials. Hence, it is concluded that the iron oxide formed in the polymer-like structure which were the desired form of Fe_3O_4 particles.[35]

3.2. Study of spectrophotometric and fluorescence spectra of the MNPs-PDNPs/RhB/FA nanoparticles

Spectrophotometric and fluorescence spectra of the MNPs-PDNPs/RhB and MNPs-PDNPs/RhB/FA nanoparticles are presented in Fig. 2. The MNPs-PDNPs/RhB have two shape absorption peaks at 259 nm and 555 nm and three broad peaks at 354 nm, 400 nm, and 513 nm. Peaks around 257 nm, 353 nm, and 553 nm are regarded as the characteristic absorption peaks of RhB molecules. However, the MNPs-PDNPs/RhB/FA nanoparticles showed absorption bands around 259 nm, 366 nm, 513 nm, and 555 nm. The absorbance band of 259 nm is arisen by the n–π* transition whereas the π–π* electron transition is produced a fluorescence peak at 553 nm (Fig. 2a). It seems that a sharp peak of RhB at the 259 nm overlaps the FA absorbance band and another technique (*i.e.* FTIR) is needed to confirm the attachment of FA to the MNPs-PDNPs/RhB (Fig. S4†).

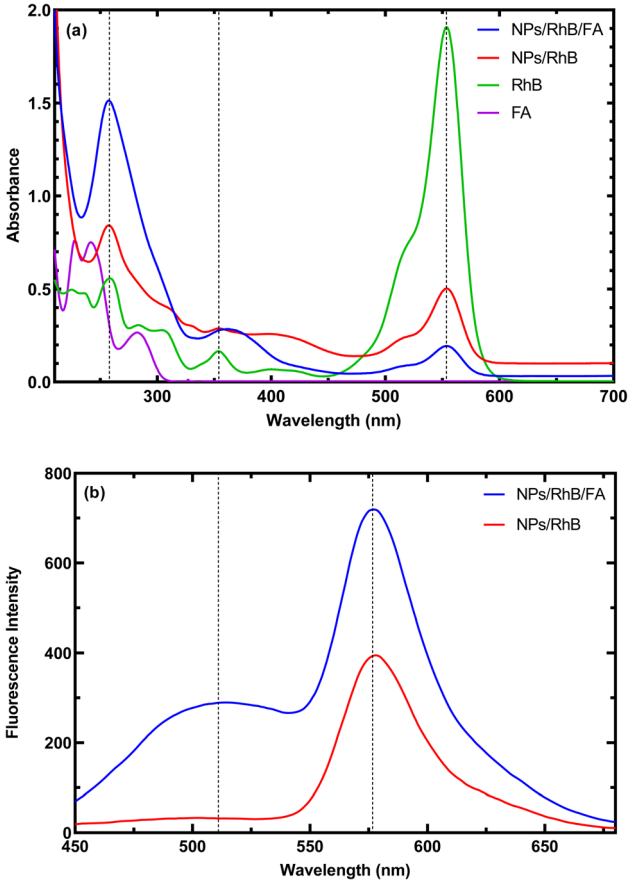

Fig. 2 (a) Absorbance, and (b) fluorescence emission spectra of the MNPs-PDNPs/RhB and MNPs-PDNPs/RhB/FA nanoparticles.

As above-mentioned, the π–π* electron transition with an absorbance wavelength of 555 nm is responsible for the photoluminescence of the MNPs-PDNPs/RhB/FA nanoparticles. The fluorescence spectra of MNPs-PDNPs/RhB/FA nanoparticles have two main peaks at 520 nm and 576 nm corresponding to the FA and RhB molecules, respectively. However, the RhB maximum peak was remained unchanged at both MNPs-PDNPs/RhB and MNPs-PDNPs/RhB/FA nanoparticles (Fig. 2b). The excitation and emission spectra of the MNPs-PDNPs/RhB/FA nanoparticles are presented in Fig. S7.† By altering the excitation wavelength in the range of 380 nm to 470 nm, the photoluminescence emission MNPs-PDNPs/RhB/FA nanoparticles were decreased and the maximum intensity was obtained at 420 nm. Furthermore, the emission peak of the MNPs-PDNPs/RhB/FA nanoparticles was 60 nm shifted to shorter wavelengths (Fig. S8†). Multiple excited states and the lower relaxation rates of the environments can result in the alteration of emission wavelength.[36,37]

3.3. Effect of pH value on the fluorescence and absorbance spectra of the MNPs-PDNPs/RhB/FA

The presence of different functional groups on the surface of MNPs-PDNPs/RhB/FA makes them be affected by the pH condition of the media. Therefore, both fluorescent and absorption spectra of MNPs-PDNPs/RhB/FA are changed by pH alerting (Fig. 3). The absorbances of MNPs-PDNPs/RhB/FA are enhanced upon increasing pHs up to 7.5 and then was constant up to about pH 9.5. However, a 10 nm blue shift was obtained at the maxima of 259 nm of the MNPs-PDNPs/RhB/FA, showing the participation of the functional groups in the formation of hydrogen bonds. In addition, fluorescence spectra of the MNPs-PDNPs/RhB/FA were influenced by pH. Fig. 3b and S9† show that the fluorescence emissions were enhanced up to pH 7.5, while the emission wavelength remained constant at all pHs. This trend is the same for both absorbance and fluorescence emission spectra. The π–π interactions are dominated at low pH values is a result of the amine groups protonation of the PDNPs. However, at the higher pHs, the π–π interactions are blocked at large scale by the free amine groups.[38]

3.4. Analytical performance of the established probe for calcium sensing

3.4.1. Influence of some factors on the fluorescence emission of nanomaterial. In this work, the effect of the pH, buffer type, buffer concentration, time of incubation, and the concentration of MNPs-PDNPs/RhB/FA was tested on the quenching intensity by Ca ions.[39] Fig. S10a† shows that the quenching effect of the Ca ions is at the maximum levels at pH

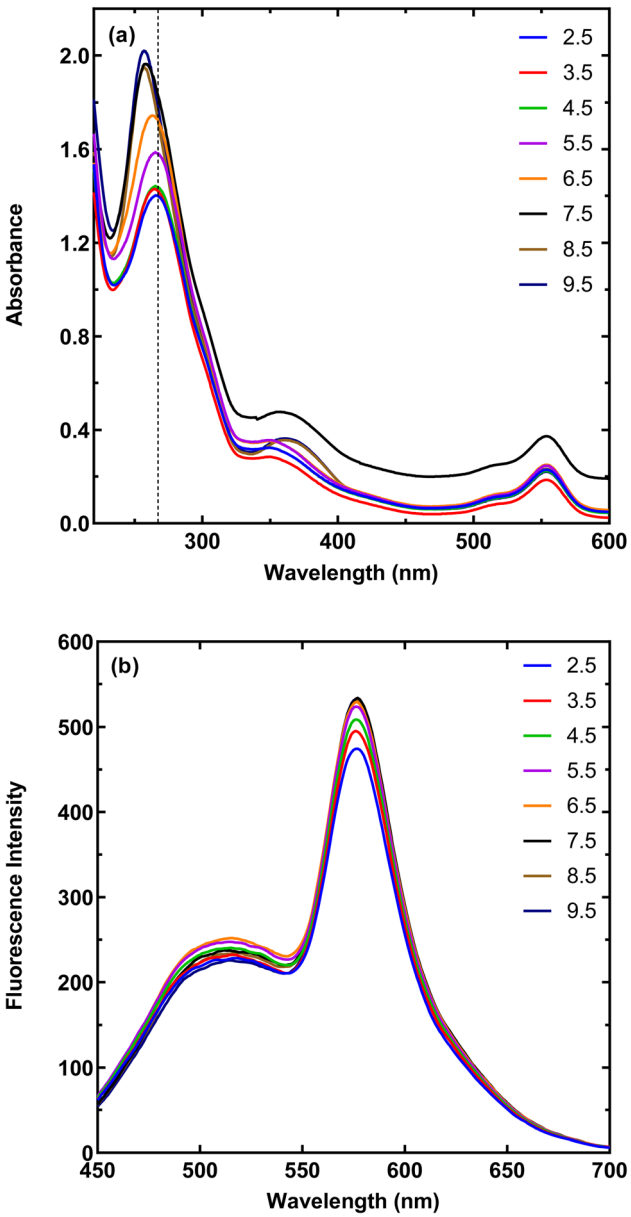

Fig. 3 Effect of pH on the (a) absorbance and (b) fluorescence spectra of the MNPs-PDNPs/RhB/FA.

7. These results caused by the protonation of amine groups in the acidic media, decreasing the interactions between Ca ions and the MNPs-PDNPs/RhB/FA. In higher pHs, calcium ions are partially or completely converted to their hydrolyzed forms ($Ca(OH)_2$). Regarding all of the obtained results, pH 7 was selected as the optimized condition to maximize the interaction between both amine groups and calcium ions (Fig. S10a†).

The type of buffer and its concertation has a massive effect on the amount of the quenched fluorescence intensity. Findings proposed that Tris buffer with a concentration of 25 mM is the best choice for the calcium ions and MNPs-PDNPs/RhB/FA interactions (Fig. S10b and c†). Fig. S10d† demonstrates the effects of the MNPs-PDNPs/RhB/FA concentrations on the measuring of Ca. The interactions between MNPs-PDNPs/RhB/FA and Ca ions may be decreased at the low concentrations of the nanoparticles.

3.4.2. Analytical figures-of-merit. The calibration curve of the quenching effect of the Ca ions on the MNPs-PDNPs/RhB/FA was plotted. For this aim, different amounts of calcium ions were added to the MNPs-PDNPs/RhB/FA under the optimized conditions and then the ΔF values were recorded as the difference between the fluorescence intensity in the presence and the absence of different levels of calcium ions. ΔF ($=F_0 - F_1$) is the analytical final that F_0 and F_1 denote to the fluorescence emission of MNPs-PDNPs/RhB/FA in the absence and presence of the calcium ions, respectively.

The calibration curve of the calcium determination is presented in Fig. 4 in which the fluorescence emission of the MNPs-PDNPs/RhB/FA has decreased upon the addition of calcium ions from 20 ng mL^{-1} to 100 ng mL^{-1} and 0.5 μg mL^{-1} to 20 μg mL^{-1}. The calibration equations of the probe at the obtained two ranges are $\Delta F = 197.4\ (\pm 9.327)\ C\ (\mu g\ mL^{-1}) + 7.007\ (\pm 0.5479)$ (p-value < 0.0022) and $\Delta F = 2.558\ (\pm 0.0969)\ C\ (\mu g\ mL^{-1}) + 30.37\ (\pm 1.058)$ (p-value < 0.0001) with correlation coefficients (R^2) of 0.9956 and 0.9943, respectively. The lower limit of detection of the probe is 20 ng mL^{-1} which covers the concentration of Ca in environmental samples. Also, the limit of detection (LOD) and limit of quantification (LOQ) of the probe were estimated to be 0.01 ng mL^{-1} and 0.033 ng mL^{-1}, respectively, based on their classical definition as $LOD = 3S_d/a$ and $LOQ = 10S_d/a$. Here, "S_d" and "a" are the slope of the calibration curve and standard deviation of the blank, respectively. The quenched fluorescence of the MNPs-PDNPs/RhB/FA probe is proportionally quenched with calcium concentrations. Table S2† lists the figures-of-merits of some of the spectroscopic probes for calcium measurement.[40–46] As seen, the developed MNPs-PDNPs/RhB/FA-based probe can detect calcium ions at a wide dynamic range with acceptable

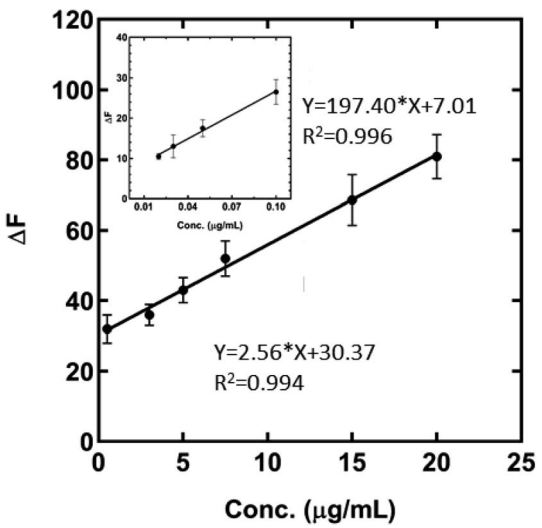

Fig. 4 Calibration curve for the determination of Ca ions in cell lysates and water samples. (Conditions; pH = 7, concentration of Tris buffer = 25 mM, time = 15 s, room temperature, and volume of the nanoparticles = 150 μL).

sensitivity. However, the developed method is able to detect calcium ions in live-cell media.

Table 1 collects the repeatability accuracy and recovery finding of the developed probe for the determination of calcium ions. These tests were investigated at three concentration levels of 0.02, 5, and 15 μg mL^{-1}. The repeatability of the probe is between 6.7–16.0% as the relative standard deviation (RSD%). However, the accuracy of the developed method ranged from 83.0 to 99.8%. In this work, all validations were done using the food and drug administration (FDA) guidelines.[39]

3.5. Specificity investigation

The specificity of the developed method was checked regarding FDA guidelines.[39] Based on the FDA guidelines, the signal of the probe was recorded in the presence and absence of the co-existing agents and reported as RSD%. The effect of some agents of Al^{3+}, Hg^{2+}, Cd^{2+}, Zn^{2+}, Se^{4+}, Cr^{2+}, Ni^{2+}, Fe^{3+}, Cu^{2+}, and Co^{2+} was investigated on the signal of the MNPs-PDNPs/RhB/FA probe to check the selectivity of the established method (Fig. S11†). The selectivity of the developed probe was measured by comparing the fluorescent intensity of the probe in the presence and absence of the interfering agents. Obtained results revealed that the fluorescence emission of the MNPs-PDNPs/RhB/FA probe was not significantly affected by the tested agents and all RSD% values are in the FDA-permitted range. The high specificity of the MNPs-PDNPs/RhB/FA probe toward calcium ions could be a consequence of interactions between the surface carboxylic acid and amine groups of MNPs-PDNPs/RhB/FA and vacant orbitals of calcium ions. Also, the size of ions and the type of vacant orbitals are other factors that affect the interaction between ions and nanoparticles.

3.6. Application of the probe

3.6.1. Detection of calcium in water samples. The developed MNPs-PDNPs/RhB/FA-based probe was used for the water samples determination from various sources. Table 2 collects the measured concentrations of calcium ions in the water samples from diverse sources (such as tap water, mineral water, and Aras river). It is noteworthy that all water samples were filtered before determination wit.

3.6.2. Detection of calcium ions in cell lysate samples. The use of the MNPs-PDNPs/RhB/FA-based probe was also checked in cell lysates. Briefly, MCF 7 cells were incubated with different calcium concentrations of 1, 10, 15, 25, and 50 μg mL^{-1}. After about 4 h incubation, the uptake of calcium ions was measured by the developed probe after a digestion step. From Fig. S12,† it is obvious that the uptake percentage was enhanced by increasing the incubated concentrations. The obtained results are in agreement with the fluorescence images. The fluorescence emission of the MNPs-PDNPs/RhB/FA was quenched by the uptake of calcium ions and the intensity of the captured images was decreased by an increase of the calcium ions. Any increase in the concentration of the calcium ions makes more interaction between the ions and nanoparticles, resulting in the diminished fluorescence intensity of the nanoparticles. It is noteworthy that the obtained quenching data points are provided at room temperature.

Table 2 Determination of calcium levels in real samples using MNPs-PDNPs/RhB/FA-based probe

Type of water	Obtained concentration (μg mL^{-1})
Tap 1	22.92 (±1.8)
Tap 2	24.68 (±7.4)
Mineral	24.68 (±1.3)
Aras river	19.12 (±4.6)

3.7. Bioimaging of cancer cells

3.7.1. Cytotoxicity and bio-imaging. The well-known 3-(4,5-dimethylthiazol-2-yl)-2,5-diphenyltetra-zolium bromide assay (MTT assay) was used to determine the cytotoxicity of MNPs-PDNPs/RhB/FA in MCF 7 cancer lines (as a FR-positive cell). A dose and time-dependent study were carried out by incubating MCF 7 cell line with (5, 10, 50, 100, 250, and 500 μg mL^{-1}) NPs for 6, 24, and 48 h, and changes in cell viability are displayed in Fig. S13.† First, it can be noticed that no significant decline in cell viability up to the NPs concentration of 500 μg mL^{-1} with respect to control. However, the increasing incubation time to 48 h minimal decreased the survival rate of cells, which was around 87% (±1.8). Overall, these results clearly demonstrated that prepared NPs show non-toxicity up to 500 μg mL^{-1} in MCF 7 cells. Thus, this study concludes that as-synthesized MNPs-PDNPs/RhB/FA nanoparticles had good biocompatibility behavior against MCF 7 cells and could be utilized for further investigations *in vivo* tests.

In addition, exclusively fluorescence bio-imaging of MCF 7 cells was carried out with NPs and obtained images are displayed in Fig. 5. The attachment of the FA molecules on the surface of MNPs-PDNPs/RhB makes them as a smart material that attaches to the FRs of the cancer cell membrane. This ability was evaluated by incubation of the cells at various concentrations and times. No fluorescence emission was observed for cells without treatment. Further, the addition of

Table 1 Repeatability and recovery of the developed approach for the Ca ion detection

Nominal concentration (μg mL^{-1})	Intraday precision (RSD%)	Interday precision (RSD%)	Intraday accuracy (RE%)	Interday accuracy (RE%)
0.02	6.7	16.0	85.0	83.0
5.0	1.0	13.0	98.8	88.0
15.0	10.5	15.0	99.8	93.0

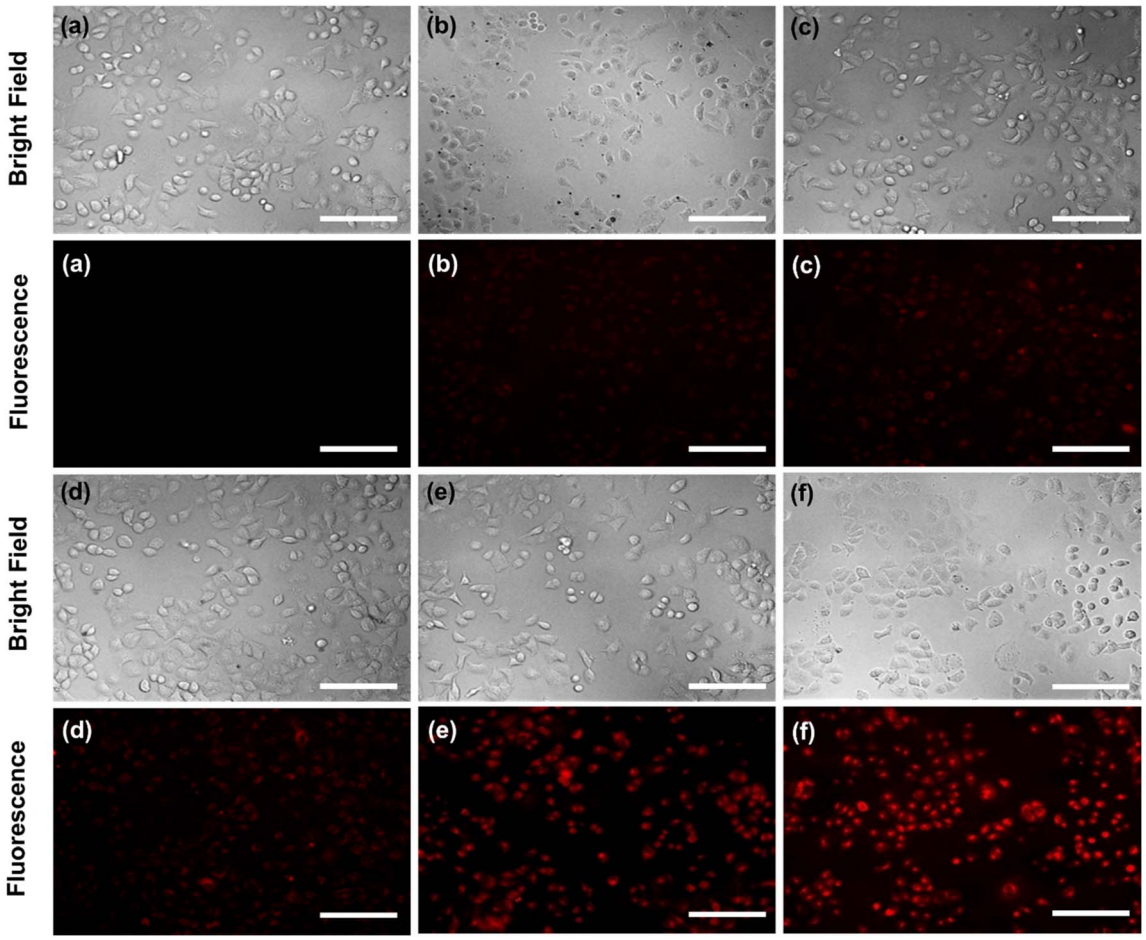

Fig. 5 Effect of the concertation of the MNPs-PDNPs/RhB/FA ((a) control, (b) 25 μg mL^{-1}, (c) 50 μg mL^{-1}, (d) 100 μg mL^{-1}, (e) 150 μg mL^{-1}, and (f) 225 μg mL^{-1}) (scale bar = 100 μm).

different concentrations of NPs with MCF 7 cells exhibits the difference in the fluorescence image (Fig. 5). Fig. 5 depicts the uptake of the MNPs-PDNPs/RhB/FA with concentrations of 25, 50, 100, 150, and 225 μg mL^{-1}. From the results, it is clear that after incubation of the cells with 225 μg mL^{-1} of the MNPs-PDNPs/RhB/FA, the fluorescence intensity of the images reached its highest level. Fig. 6 shows the fluorescence bio-images of MCF 7 cells after contact with MNPs-PDNPs/RhB/FA nanoparticles in a time-dependent study. The 4 h of the incubation time shows bright fluorescence cell images when compared to 1 and 3 h of the incubation due to the high penetration NPs into the MCF 7 cells. The efficiency of MNPs-PDNPs/RhB/FA uptake to FR-positive cells was increased by the time of incubation. Bright red emission of MNPs-PDNPs/RhB/FA was mainly observed in the surface membrane of MCF 7 cells and cytoplasm, whole the nucleus was not significantly affected by the materials, demonstrating that the MNPs-PDNPs/RhB/FA is firstly attached to FRs and then gradually enter into the cells' cytoplasm of cells. These results confirmed that FRs are placed at the surface membrane of the FR-overexpressed cells. As seen, the cell morphology was not significantly affected by the MNPs-PDNPs/RhB/FA.

The targeting specificity of the MNPs-PDNPs/RhB/FA was also studied by incubation of the HEK 293 cells with nanoparticles.[47] Results proposed that the MNPs-PDNPs/RhB/FA failed to attach to the FR-negative cells due to the lower expression of FRs on the membrane of HEK 293 than MCF 7 cells (Fig. S14†). The extraordinary affinity of MNPs-PDNPs/RhB/FA to the MCF 7 cells is predominantly triggered by the high formation constant of FA/FR (10^{+8} to 10^{+9} M^{-1}).[48] The high formation constants enhance the targeted interactions and the specificity of the bioimaging of the cells.

3.7.2. Quantification of Ca ions intracellular levels in live cells. To determine the intracellular levels of calcium ions, the MCF 7 cancer cells were incubated with different concentrations of calcium ions (5, 20, and 50 μg mL^{-1}) for 6 h. After washing with PBS to remove the remaining calcium ions, the treated cells were incubated with MNPs-PDNPs/RhB/FA nanoparticles in culture media for 4 h at 37 °C. The incubated cells were imaged by fluorescence microscopy (Fig. 7). The intensity of the images was compared with the control groups which only incubated with the MNPs-PDNPs/RhB/FA nanoparticles. Generally, the calcium-treated cells exhibited lower emitted fluorescence due to the quenching effect of calcium ions. These results established that the MNPs-PDNPs/RhB/FA-based probe

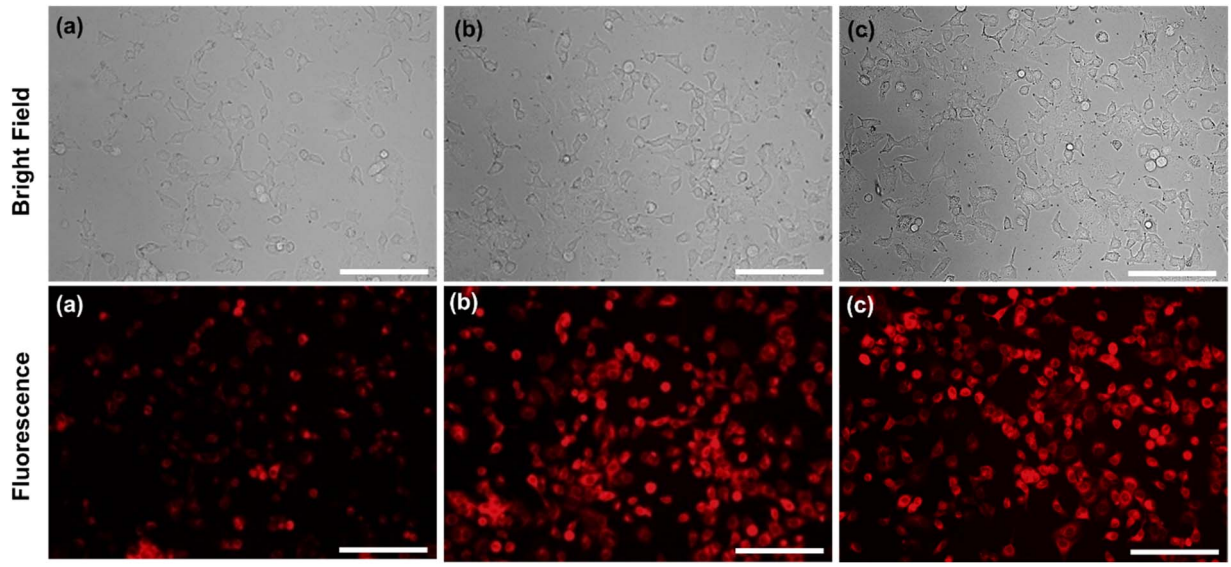

Fig. 6 Effect of the time of incubation (a) 1 h, (b) 3 h, and (c) 4 h on the amount the cell uptake value (scale bar = 100 μm).

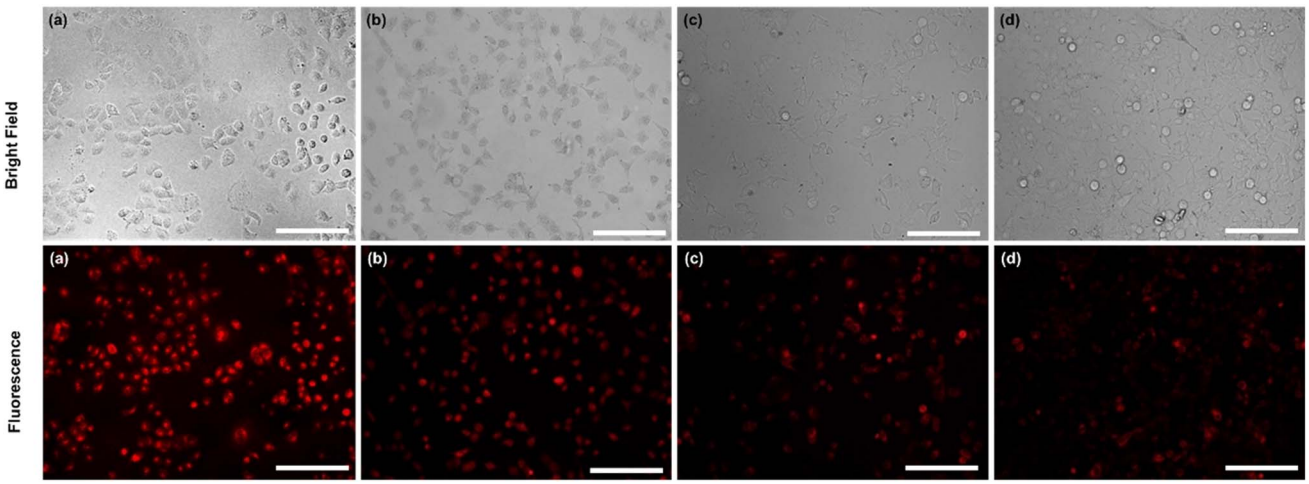

Fig. 7 Detection of the intracellular concertation of Ca ions (a) control group, (b) 5 μg mL^{-1}, (c) 20 μg mL^{-1}, and (d) 50 μg mL^{-1} (scale bar = 100 μm).

can detect the intracellular calcium ions in live cells with favorable accuracy.

4. Conclusion

A novel MNPs-PDNPs/RhB/FA nanocomposite was produced and used for the quantification of calcium ions in water samples and live cells. Also, it was employed for the targeting of FR-positive MCF 7 cancer cells. The cell viability of MNPs-PDNPs/RhB/FA nanoparticles was tested by the MTT assay with a biocompatible nature even at the 225 μg mL^{-1} concentration. Obtained results confirmed that the MNPs-PDNPs/RhB/FA nanoparticles can be uptake into the FR-positive cancer cells through FA/FR interactions with exceptional selectivity. In addition, the MNPs-PDNPs/RhB/FA was utilized for the detection of calcium ions in water samples and live cells with LLOQ of as low as around 20 ng mL^{-1}. Bright and high fluorescence emission of the probe provides a more sensitive method for Ca detection. Furthermore, the emission wavelength is in the visible area, reducing the self-absorption of the fluorescence emission of the nanoparticles. Also, low-emission wavelengths reduce photobleaching and enhance the stability of the nanoparticles. In addition, high energy wavelengths may be harmful to the living cell. The applicability of this sensor was checked in the detection of calcium ions in the real samples which are collected from various sources and the detection of calcium ions in live cells. However, the application of this sensor may be limited in presence of some ions as studied in the main text.

Conflicts of interest

There is no conflict of interest.

Acknowledgements

The authors would like to acknowledge the financial supports from Tabriz University of Medical Sciences (Tabriz, Iran) (grant number: 67984).

References

1 A. T. Harootunian, J. P. Kao, S. Paranjape and R. Y. Tsien, *Science*, 1991, **251**, 75–78.
2 R. Sangubotla and J. Kim, *TrAC, Trends Anal. Chem.*, 2018, **105**, 240–250.
3 E. Pchitskaya, E. Popugaeva and I. Bezprozvanny, *Cell Calcium*, 2018, **70**, 87–94.
4 K. Reddy, C. L. Cusack, I. C. Nnah, K. Khayati, C. Saqcena, T. B. Huynh, S. A. Noggle, A. Ballabio and R. Dobrowolski, *Cell Rep.*, 2016, **14**, 2166–2179.
5 G. A. Weyhenmeyer, J. Hartmann, D. O. Hessen, J. Kopáček, J. Hejzlar, S. Jacquet, S. K. Hamilton, P. Verburg, T. H. Leach, M. Schmid, G. Flaim, T. Nõges, P. Nõges, V. C. Wentzky, M. Rogora, J. A. Rusak, S. Kosten, A. M. Paterson, K. Teubner, S. N. Higgins, G. Lawrence, K. Kangur, I. Kokorite, L. Cerasino, C. Funk, R. Harvey, F. Moatar, H. A. de Wit and T. Zechmeister, *Sci. Rep.*, 2019, **9**, 10450.
6 Z. Golsanamlou, J. Soleymani, S. Abbaspour, M. Siahi-Shadbad, E. Rahimpour and A. Jouyban, *Spectrochim. Acta, Part A*, 2021, **256**, 119747.
7 J. Soleymani, V. Shafiei-Irannejad, M. R. Hamblin, M. Hasanzadeh, M. H. Somi and A. Jouyban, *Mater. Sci. Eng. C*, 2021, **121**, 111691.
8 M. Moirangthem, R. Arts, M. Merkx and A. P. H. J. Schenning, *Adv. Funct. Mater.*, 2016, **26**, 1154–1160.
9 A. Takahashi, P. Camacho, J. D. Lechleiter and B. Herman, *Physiol. Rev.*, 1999, **79**, 1089–1125.
10 J. Wu, L. Liu, T. Matsuda, Y. Zhao, A. Rebane, M. Drobizhev, Y.-F. Chang, S. Araki, Y. Arai, K. March, T. E. Hughes, K. Sagou, T. Miyata, T. Nagai, W. Li and R. E. Campbell, *ACS Chem. Neurosci.*, 2013, **4**, 963–972.
11 I. Isildak, F. Navaeipour, H. Afsharan, G. S. Kanberoglu, I. Agir, T. Ozer, N. Annabi, E. E. Totu and B. Khalilzadeh, *Microchim. Acta*, 2020, **187**, 25.
12 B. Khalilzadeh, N. Shadjou, H. N. Charoudeh and M.-R. Rashidi, *Microchim. Acta*, 2017, **184**, 3651–3662.
13 B. Khalilzadeh, M. Rashidi, A. Soleimanian, H. Tajalli, G. S. Kanberoglu, B. Baradaran and M.-R. Rashidi, *Int. J. Biol. Macromol.*, 2019, **134**, 695–703.
14 J. Soleymani, D. Perez-Guaita, M. Hasanzadeh, N. Shadjou and A. Jouyban, *TrAC, Trends Anal. Chem.*, 2017, **86**, 122–142.
15 J. L. Manzoori, M. Amjadi, J. Soleymani, E. Tamizi, A. Rezamand and A. Jouyban, *Luminescence*, 2012, **27**, 268–273.
16 M. Hasanzadeh, M. Feyziazar, E. Solhi, A. Mokhtarzadeh, J. Soleymani, N. Shadjou, A. Jouyban and S. Mahboob, *Microchem. J.*, 2019, **145**, 778–783.
17 H. Yumak, B. Ozturk, J. Sheng and M. V Yigit, *Langmuir*, 2015, **31**, 9943–9952.
18 S. Jafarzadeh, N. Bargahi, H. B. Shamloo and J. Soleymani, *RSC Adv.*, 2022, **12**, 8492–8501.
19 J. Soleymani, S. Azizi, S. Abbaspour-Ravasjani, M. Hasanzadeh, M. H. Somi and A. Jouyban, *Microchem. J.*, 2021, **170**, 106732.
20 X. Zhao, H. Li and R. J. Lee, *Expert Opin. Drug Delivery*, 2008, **5**, 309–319.
21 X. Zhao, R. Shen, L. Bao, C. Wang and H. Yuan, *Carbohydr. Polym.*, 2020, **245**, 116509.
22 B. Farran, E. Pavitra, P. Kasa, S. Peela, G. S. Rama Raju and G. P. Nagaraju, *Cytokine Growth Factor Rev.*, 2019, **45**, 45–52.
23 J. Soleymani, M. Hasanzadeh, M. H. Somi and A. Jouyban, *Mater. Sci. Eng. C*, 2020, **107**, 110320.
24 J. Soleymani, M. Hasanzadeh, N. Shadjou, M. H. Somi and A. Jouyban, *J. Pharm. Biomed. Anal.*, 2020, **180**, 113077.
25 M. Wang, Y. Liang, Z. Zhang, G. Ren, Y. Liu, S. Wu and J. Shen, *Anal. Chim. Acta*, 2019, **1086**, 122–132.
26 S. Damiati, M. Peacock, R. Mhanna, S. Søpstad, U. B. Sleytr and B. Schuster, *Sens. Actuators, B*, 2018, **267**, 224–230.
27 G. E. Gu, C. S. Park, H.-J. Cho, T. H. Ha, J. Bae, O. S. Kwon, J.-S. Lee and C.-S. Lee, *Sci. Rep.*, 2018, **8**, 4393.
28 X. Liu, J. Cao, H. Li, J. Li, Q. Jin, K. Ren and J. Ji, *ACS Nano*, 2013, **7**, 9384–9395.
29 Q. Lin, X. Huang, J. Tang, Y. Han and H. Chen, *J. Nanopart. Res.*, 2013, **15**, 2144.
30 R. Nisticò, F. Cesano and F. Garello, *Inorganics*, 2020, **8**, 6.
31 W. Zhang, S. Wang, J. Ji, Y. Li, G. Zhang, F. Zhang and X. Fan, *Nanoscale*, 2013, **5**, 6030–6033.
32 Y. Fang, A. Zhou, W. Yang, T. Araya, Y. Huang, P. Zhao, D. Johnson, J. Wang and Z. J. Ren, *Sci. Rep.*, 2018, **8**, 229.
33 M. J. E. Fischer, N. J. Mol and M. J. E. Fischer, *Amine Coupling Through EDC/NHS: A Practical Approach BT - Surface Plasmon Resonance: Methods and Protocols*, Humana Press, Totowa, NJ, 2010, pp. 55–73.
34 N. Mufti, D. R. P. Sari, A. F. Muyasaroh and A. Taufiq, *Journal of Physics: Conference Series*, IOP Publishing, 2020, vol. 1595, p. 12004.
35 Z. Ma, Y. Guan and H. Liu, *J. Polym. Sci., Part A: Polym. Chem.*, 2005, **43**, 3433–3439.
36 P. Suppan, *Chemistry and Light*, The Royal Society of Chemistry, London, UK, 1994.
37 M. Józefowicz and J. R. Heldt, *J. Fluoresc.*, 2011, **21**, 239–245.
38 S. Bevers, T. P. O'De and L. W. McLaughlin, *J. Am. Chem. Soc.*, 1998, **120**, 11004–11005.
39 Food and Drug Administration (FDA), *FDA guidelines*, **https://www.fda.gov/downloads/Drugs/Guidances/ucm070107.pdf**, accessed 16 September 2021.
40 J. Yue, L. Li, L. Cao, M. Zan, D. Yang, Z. Wang, Z. Chang, Q. Mei, P. Miao and W.-F. Dong, *ACS Appl. Mater. Interfaces*, 2019, **11**, 44566–44572.
41 E. Babaee, A. Barati, M. B. Gholivand, A. Arman, A. A. Taherpour, N. Zolfaghar and M. Shamsipur, *J. Hazard. Mater.*, 2019, **367**, 437–446.
42 S. R. Ankireddy and J. Kim, *Highly Selective and Sensitive Detection of Calcium (II) Ions in Human Serum Using Novel Fluorescent Carbon Dots*, Elsevier B.V., 2018, vol. 255.
43 L. Lu, X. An and W. Huang, *Anal. Methods*, 2017, **9**, 23–27.

44 H. Chen, J. Peng, L. Yu, H. Chen, M. Sun, Z. Sun, R. Ni, K. A. Alamry, H. M. Marwani and S. Wang, *J. Fluoresc.*, 2020, **30**, 463–470.
45 S. Ghosh, Y. Chen, A. George, M. Dutta and M. A. Stroscio, *Front. Chem.*, 2020, **8**, 1–9.
46 Z. Liu, X. Jing, S. Zhang and Y. Tian, *Anal. Chem.*, 2019, **91**, 2488–2497.
47 K. Pal, A. Heinsch, A. Berkessel and A. L. Koner, *Chem.–Eur. J.*, 2017, **23**, 15008–15011.
48 M. D. Salazar and M. Ratnam, *Cancer Metastasis Rev.*, 2007, **26**, 141–152.